Contents lists available at ScienceDirect

Additive Manufacturing

Research Paper

Additively manufactured ultra-high vacuum chamber for portable quantum technologies

N. Cooper [a,*], L.A. Coles [b,*], S. Everton [b], I. Maskery [d], R.P. Campion [a], S. Madkhaly [a], C. Morley [a], J. O'Shea [a], W. Evans [c], R. Saint [c], P. Krüger [c], F. Oručević [c], C. Tuck [b,d], R.D. Wildman [b,d], T. M. Fromhold [a], L. Hackermüller [a]

[a] School of Physics and Astronomy, University of Nottingham, NG7 2RD, UK
[b] Added Scientific Ltd., Isaac Newton Centre, Nottingham Science Park NG7 2RH, UK
[c] Department of Physics and Astronomy, University of Sussex, Brighton BN1 9QH, UK
[d] Centre for Additive Manufacturing, Faculty of Engineering, University of Nottingham, NG7 2RD, UK

ARTICLE INFO

ABSTRACT

Additive manufacturing is having a dramatic impact on research and industry across multiple sectors, but the production of additively manufactured systems for ultra-high vacuum applications has so far proved elusive and widely been considered impossible. We demonstrate the first additively manufactured vacuum chamber operating at a pressure below 10^{-10} mbar, measured via an ion pump current reading, and show that the corresponding upper limit on the total gas output of the additively manufactured material is 3.6×10^{-13} mbar l/(s mm^2). The chamber is produced from AlSi10Mg by laser powder bed fusion. Detailed surface analysis reveals that an oxidised, Mg-rich surface layer forms on the additively manufactured material and plays a key role in enabling vacuum compatibility. Our results not only enable lightweight, compact versions of existing systems, but also facilitate rapid prototyping and unlock hitherto inaccessible options in experimental science by removing the constraints that traditional manufacturing considerations impose on component design. This is particularly relevant to the burgeoning field of portable quantum sensors — a point that we illustrate by using the chamber to create a magneto-optical trap for cold ^{85}Rb atoms — and will impact significantly on all application areas of high and ultra-high vacuum.

1. Introduction

We demonstrate that additive manufacturing (AM) is suitable for the production of ultra-high vacuum (UHV) equipment, thus opening up opportunities for rapid prototyping, weight reduction and enhanced functionality across the high and ultra-high vacuum sectors.

Applications of UHV systems are numerous, ranging from established technologies such as photosensors, cameras, cryostats, electron microscopes and x-ray photoelectron spectroscopy (XPS) analyzers to important emerging research areas such as portable quantum sensors based on cold atoms [1–4]. AM methods could accelerate both fundamental research and technological development across all of the above areas, by allowing substantial reductions in the size, weight and development lead time of the associated UHV apparatus. For example, the UHV chamber described here, which is fabricated via a laser powder bed fusion (LPBF)

technique [5] from aluminium alloy AlSi10Mg, weighs just 245 g — 70% less than equivalent standard chambers. Such mass reduction is particularly critical for space-based applications of UHV, for example experimental tests of fundamental physics using space-borne quantum sensors [6–9].

However, despite recent advances in AM processing of metals [10, 11], a complete UHV chamber is yet to be produced via AM. Identified challenges for vacuum compatibility are surfaces roughness, porosity and limited hardness. Rough surfaces are associated with increased outgassing rates, porosity [12,13] can create leaks or virtual leaks from trapped gas-pockets and limited hardness [10] reduces the effectiveness of traditional knife-edge seals at vacuum connections.

These characteristics of AM metals have led to legitimate doubts as to their suitability for the production of UHV components. The alloy AlSi10Mg offers a higher thermal conductivity than alternatives such as

---

titanium or stainless steel, which may help to improve uniformity and reduce build defects when printing. Here, we conduct a detailed analysis of the surface of AM AlSi10Mg, employing optical and electron microscopy, mass spectrometry and x-ray photoelectron spectroscopy. This not only reveals a material structure free from significant porosity or lateral cracking, but also that the surface chemistry associated with AM AlSi10Mg is critical to obtaining high vacuum performance — specifically that a heavily oxidized, Mg-rich layer on the surface of the AM material strongly suppresses the outgassing of magnesium from the material bulk. As a result, the chamber described herein readily sustains a pressure below 10^{-10} mbar.

This vacuum performance is more than sufficient to permit the capture of a cloud of cold ^{85}Rb atoms in a magneto-optical trap (MOT) [14], as shown in Fig. 1(b); MOTs are the starting point for nearly all cold-atom based experiments and devices. These include atomic clocks for precision timekeeping [15–17], high-precision gravimeters for applications in geology, navigation and civil engineering [18–20] and cold atom magnetometers [21,22] for navigation and medical imaging. This important and burgeoning field stands to benefit strongly from the application of AM methods to UHV equipment..

Although there are prior examples of AM materials being subject to a UHV environment [23,24], such as the conflat flange demonstrated in [24], and work towards vacuum-based applications of AM components has been conducted [25–28,29], a full vacuum chamber produced via AM methods has yet to reach the UHV regime. The chamber we demonstrate herein represents a significant increase in size and complexity over previous AM UHV components - an essential step towards the exploitation of the benefits of AM within the UHV sector. We also demonstrate the compatibility of our chamber with industry-standard components and sealing techniques, a detail that has been absent from most previous work.

2. Methods

2.1. Chamber design and manufacture

The AM UHV chamber was designed to meet the functional requirements of a magneto-optical trap (MOT) [30] — the first essential component of nearly all quantum technologies based on cold atoms. These requirements are: optical access for three orthogonal beam pairs, magnetic coils, a UHV environment and the ability to connect to standard components, such as vacuum pumps — see Fig. 2.

"Design for LPBF" methodology [5] was applied to reduce the overall weight without affecting mechanical stability. Light-weighting of the chamber core was achieved by refining the port geometry and minimizing the spacing between ports. A 2.5 mm thick internal skin was added between the ports to hold the UHV, as shown in Fig. 2(b). Effort

was made to keep symmetry where possible in the chamber design, thus keeping the ports perpendicular to the optical paths under the external pressure loading. The resulting (negligible) deformation of the chamber under an external pressure load was analyzed via 'Finite Element Analysis' (FEA) based simulation using 'MSc Marc 2017.1.0′ — see Supplementary Material (Supplementary Fig. 2).

Within a predefined volume (Fig. 2(c) a variable density triply periodic minimal surface lattice was integrated with the symmetric internal core design to add a layer of robustness and increase stiffness; this took the form of a matrix based gyroid surface [31,32], as shown in Fig. 2(d). The variable volume fraction (density) of the lattice permits reinforcement of areas that need more support, such as those adjacent to the ports. The final chamber design (Fig. 2(e)) consists of multiple conflat ports (2 × CF40 ports and 8 × CF16), making it compatible with standard UHV equipment, as shown in Fig. 4(a). Building on the design approach demonstrated here, it will be possible to produce complex, multi-functional, part-consolidated chamber designs that can only be realized by AM.

Of the metallic alloys available for AM processing, which also include titanium, stainless steel and silver, aluminium alloy AlSi10Mg was selected because of its high specific strength, low density and good thermal conductivity [33]; a higher thermal conductivity allows faster dissipation of the heat generated during the LPBF process, reducing the likelihood of build imperfections occurring due to build-up of temperature gradients and the resulting thermal stresses. LPBF fabrication was chosen over alternatives such as inkjet binder printing [34] to avoid the use of any non-UHV compatible materials in the fabrication process, thus removing the possibility that incomplete burnoff might lead to contamination of the vacuum system. Materials produced by LPBF have a characteristically ultra-fine grain structure with epitaxial grain growth aligned with the build direction [35]. Solution heat treatments can be applied to homogenize the microstructure or control the grain size. These methods are often utilised to increase the ductility of the alloy; subsequently an ageing heat treatment is applied to promote precipitate hardening and increase the material strength [36,37]. The resulting material performance after the selected heat treatment regime was verified for knife edge seal repeatability and thread torque requirements — see Appendix. The Vickers hardness was measured for a machined surface (as in Fig. 3(g)) as (105 ± 0.8) HV5.

Following design and material testing the chamber was printed using a Renishaw AM250 laser powder bed fusion machine, as described in detail below.

2.1.1. Material

The pre-alloyed, gas atomised AlSi10Mg powder from TLS Technik GmbH, contains Al 89.8 wt%, Si 9.7 wt% and Mg 0.3 wt% with powder particles in the range 10 μm to 100 μm, measured using a Malvern UK
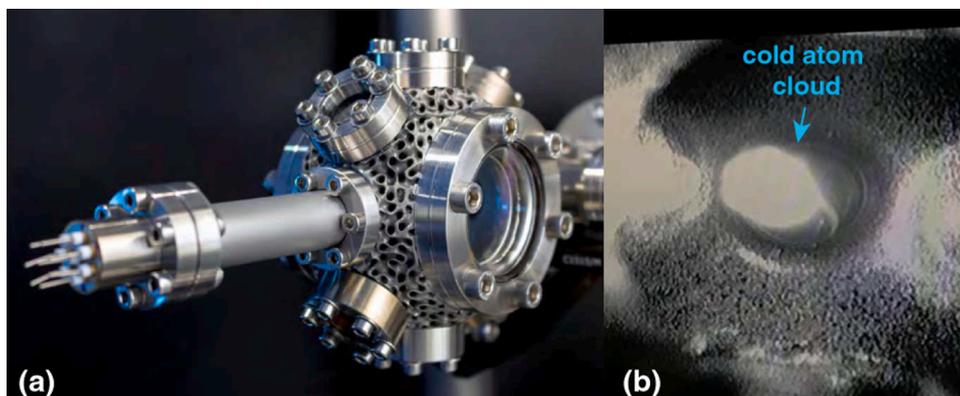
Fig. 1. An additively manufactured UHV chamber for quantum technologies (a) Photograph of the final, assembled AM-built UHV chamber with standard UHV components. For scale, the larger ports on the AM vacuum chamber are CF40 and the smaller CF16. (b) Fluorescence image of a cold cloud of ^{85}Rb atoms confined in a magneto-optical trap inside the chamber. The diameter of the atomic cloud is approximately 10 mm.
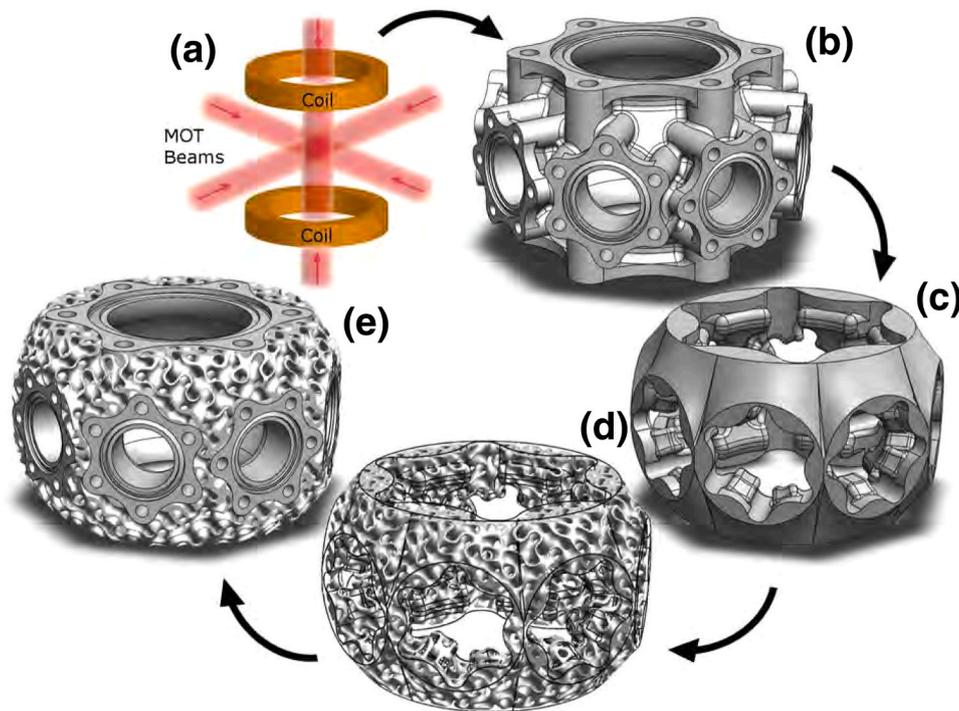
Fig. 2. Overview of the design process (a) Illustration of the functional requirements for cold atom cloud trapping. (b) Thin wall internal chamber design with conflat ports. (**c**) Volume identified for additional lattice support. (d) The variable density triply periodic minimal surface gyroid matrix lattice, which has been generated from the previous volume in (c) to add a layer of robustness and increase structural stiffness. (e) Final lightweight chamber design.

Mastersizer 3000.

2.1.2. Manufacture

A Renishaw AM250 laser powder bed fusion machine was used to manufacture all test pieces and the final vacuum chamber. The machine uses a Yb fiber laser at 1064 nm wavelength, with a laser power of 200 W, and heats the powder bed to 180 °C during build. The parts were built on an aluminium baseplate using a powder layer thickness of 25 μm. A hatch spacing of 80 μm, point distance of 70 μm and exposure time of 220 μs were selected, giving an effective scanning speed of 318 mm s^{-1}. A chequerboard pattern was used to minimise the accumulation of residual stresses and after each layer, the scan pattern was rotated by 67 degrees.

2.1.3. Post processing and mechanical machining

Once processed and removed from the build machine, the parts were stress-relieve heat treated on the build plate for 2 h at 300 °C and furnace cooled. The parts were removed from the build plate by wire electro-discharge machining and bead blasted to remove any loosely adhered powder particles. Finally, a T6-like series of heat treatments were applied to modify the microstructure of the material [36]. The components were subject to a solution heat treatment for 1 h at ~ 500 °C followed by a water quench and then aged for 6 h at ~ 150 °C. To ensure a good tolerance at the mating surfaces between the chamber interfaces and the standard off-the-shelf UHV parts, the interfaces were machined, and knife edges and threaded bolt holes added. The internal chamber surface was left in the as-built condition.

2.2. Outgassing behaviour and surface material analysis

LPBF components and materials tend to have rough surfaces [10] and have therefore been thought unsuitable for UHV applications. Fig. 3 (a) shows a focus variation microscopy (FVM) image of a 1.5 mm by 1.5 mm area on the upper surface of an unmachined test sample, built and post-processed identically to the UHV chamber. The image was obtained using an Alicona G5 Infinite Focus microscope. The surface roughness Sq, the root mean square height over the area sampled, was measured as $Sq = 5.3 \pm 0.1$ μm. Scanning Electron Microscopy (SEM) of the same surface reveals a rich surface structure with lateral features as small as 1–10 μm (Fig. 3(b, c)), but no evidence of cracks, tears or deep pores. The dense, high-quality structure of the material is also seen in SEM images of machined surfaces. Fig 3(d) shows an image of the machined knife-edge, with some machining marks but no material defects visible at this zoom level. An image taken at higher magnification (Fig. 3(e)) shows small, micrometer-sized defects aligned with the direction of the machining tool, but none orthogonal to it. This anisotropy suggests that the defects stem from the machining rather than the AM build process. Importantly, the defects seen on the machined surface are isolated and discontinuous, and no evidence of lateral cracking is observed.

To characterize the outgassing behaviour and gain information about the surface composition, we conducted a mass spectrometric study on the LPBF alloy used to build the vacuum chamber, while varying the temperature from 20 to 500°C. In addition, x-ray photo-electron spectroscopy (XPS) of a machined and unmachined surface was performed at room temperature.

The results of both measurements suggest the formation of an Mg-enriched, oxidised layer on the surface of the material, which is likely to play a role in suppressing outgassing.

Ten test samples of the LPBF material (10 × 10 × 4 mm cuboids) were fabricated using the same build parameters and feedstock as the chamber. The samples were placed in a temperature-controlled Knudsen Cell connected to a line-of-sight mass spectrometer. The molecular/atomic beam from the source can be interrupted by a rotating chopper, which allows the line of sight beam to be distinguished from background signals [38]. Scans were run across the mass range of 1–200 amu, while the material was heated up as far as 500 °C with a heating rate of 10 °C/min as shown in Fig. 4(f). The experiment was then repeated in a quasi-stable situation, holding the sample for 48 h each at temperatures of 250 °C, 350 °C, 400 °C and 450°C in turn. In both cases similar
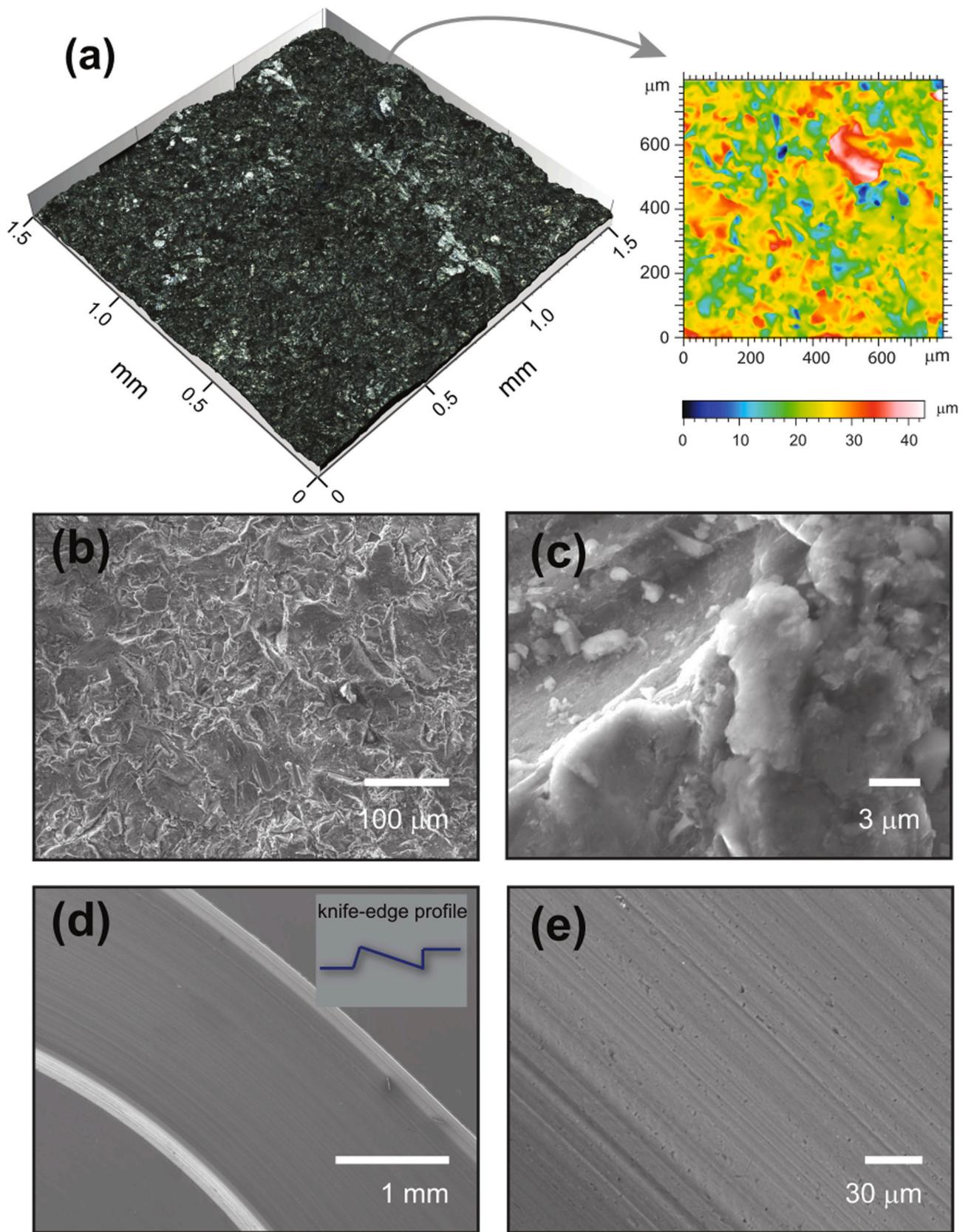
Fig. 3. Surface and material characterization (a) Focus Variation Microscopy image of the untreated surface of an additively manufactured sample of AlSi10Mg (left) and color map showing the corresponding surface profile (right). (b,c) SEM images of the untreated surface vs. (d,e) SEM images of the machined surface and knife-edge (For interpretation of the references to colour in this figure legend, the reader is referred to the web version of this article.).
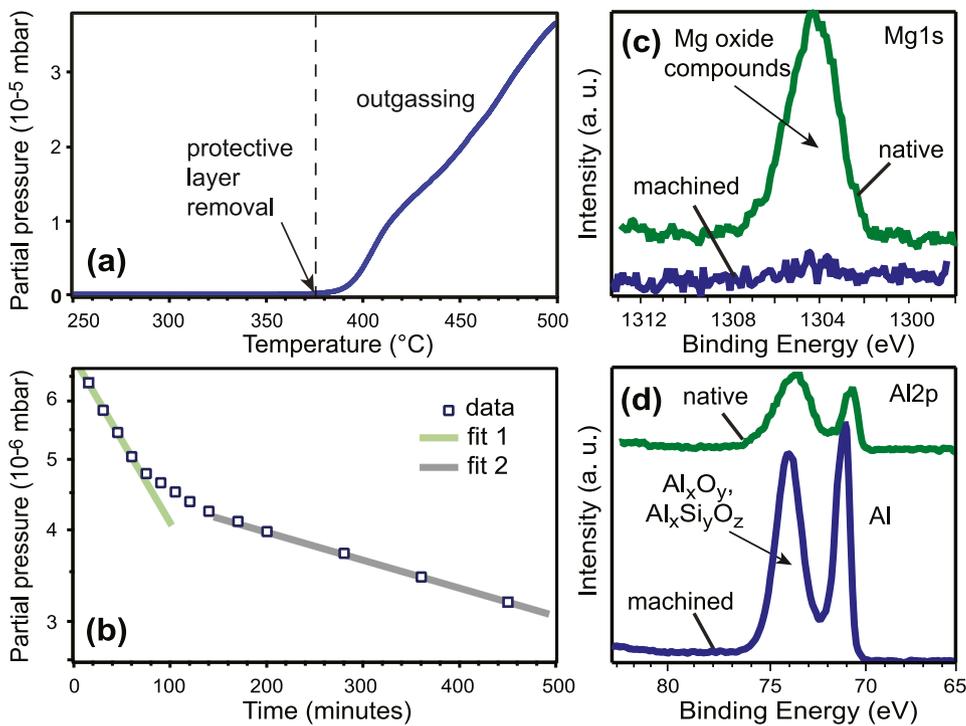
Fig. 4. Mass spectrometry results and XPS material characterisation. (a) Material characterization with mass spectrometry - partial pressure of ^{24}Mg in the Knudsen Cell as a sample of AM AlSi10Mg is heated to 500 °C at 10 °C per minute. (b) Partial pressure of ^{24}Mg in the Knudsen Cell as a function of time after a sample of AM AlSi10Mg has been heated rapidly to 420 °C and held at this temperature. Lines are linear fits at short and long timescales. (c,d) XPS spectra showing a high content of Mg oxides in the untreated surface vs. a low abundance of Mg oxides in the machined surface (c) and a similar but smaller discrepancy for Al (d). A vertical offset has been applied to improve visibility (For interpretation of the references to colour in this figure legend, the reader is referred to the web version of this article.).

behaviour was observed. Other than (expected and unavoidable) atmospheric species, the only peaks detected were for magnesium (primarily ^{24}Mg), which became evident above 400°C°C. Below 375 °C, no ^{24}Mg signal is measurable, as determined by the noise level, while above that temperature a sharp rise in the magnesium signal is visible.

If the temperature is raised above 400 °C and then subsequently decreased, the ^{24}Mg signal does not return to its original value, but remains at a considerably higher level (factor 10^3 at 350 °C). The signal then persists at temperatures far below 350°C. We interpret these results as the removal of a protective layer. The presence of this layer reduces the rate of Mg emission from the sample, and may have a similar effect on outgassing of other particle species.

This interpretation is supported by a second experiment, where samples were held at 420 °C for 150 min and the time variation of the emission was measured (see Fig. 4(g)). All samples show a rapid initial reduction in Mg emission (fit 1 in Fig. 4(g) with a gradient of $g_1 = -5.1(4)\exp(-3)$ ln(mbar)/min) followed by a much slower subsequent tail-off (fit 2 with a gradient of $g_2 = -9.1(2)\exp(-4)$ ln(mbar)/min).

For Fig. 4(f, g) the system was calibrated with a pure magnesium sample of the same dimensions as the LPBF material and the observed count rate for the LPBF samples normalised to the magnesium counts and expressed as a partial pressure.

Temperature dependent emission data taken immediately after the removal of the oxide layer can be plotted as an Arrhenius plot, resulting in a gradient proportional to the activation energy that corresponds within 1% to that of a pure magnesium sample (see Supplementary Fig. 4). Therefore the behaviour seen in Fig. 4(f) is consistent with a relatively fast removal of a protective top-surface layer leading to the exposure of a thin, unoxidised, Mg-enriched layer at the sample surface. This layer is then rapidly depleted (regime of fit 1) and Mg emission eventually becomes limited by the rate of diffusion of Mg from the bulk to the surface (regime of fit 2). A formation process for magnesium oxides at high temperatures during the LPBF build process for AlSi10Mg has been suggested in [39,40].

The measured outgassing properties of the test samples represent an average over their exposed surfaces, for which the relative representation of the different surface orientations relative to the build direction is

comparable to that of the chamber's interior; due to the complexity of the chamber's form exact correspondence was not practical. Use of the same build parameters and feedstock should ensure similar surface characteristics (e.g. grain size, surface roughness etc.) for the test samples and chamber.

XPS measurements were performed on an untreated surface of the AM material and on a machined surface of the same sample (Fig. 4(h)). The XPS data confirm the hypothesis of a surface layer with a larger content of magnesium oxides. Fig 4(h) (left) shows a peak at 1304.2 eV corresponding to magnesium oxide compounds such as MgO or Mg (OH)$_2$, illustrating the difference in abundance of Mg in the untreated surface (green line) and the machined surface (blue line). Fig 4(h) (right) features two peaks for both surfaces. The low binding energy peak around 71 eV is attributed to metallic aluminium, while the second peak with a binding energy around 74 eV is indicative of aluminium oxide or aluminosilicate [41]. The relative abundance of Si is similar on both surfaces (see Supplementary Fig. 5). From the XPS spectra the composition of the unmachined surface was determined to be 22% Mg, 69% Al and 9% Si, while the machined surface was 1% Mg, 90% Al and 9% Si, consistent with the composition of the powder within the measurement uncertainties. The high concentration of Mg on the untreated surface is remarkable, given that Mg only accounts for 0.3% of the powder composition, but consistent with the hypothesis developed above. Note that XPS only characterises the surface up to a depth of 10 nm. On both surfaces the Mg component was detected exclusively within a range of binding energies consistent with its oxidised forms, e.g. MgO and Mg (OH)$_2$, rather than pure metal [42]. By contrast, the Si and Al components were detected as pure and oxidised forms.

Both approaches confirm the existence of a layer with a high abundance of oxidised Mg at the native surface. The mass spectrometry results also demonstrate that this layer can withstand temperatures up to 350 °C and reduces the outgassing of volatile species. For high temperature applications of AM parts (e.g. for use in scanning tunneling microscopes), the development of methods to enhance the stability of this protective layer is a promising line of investigation.
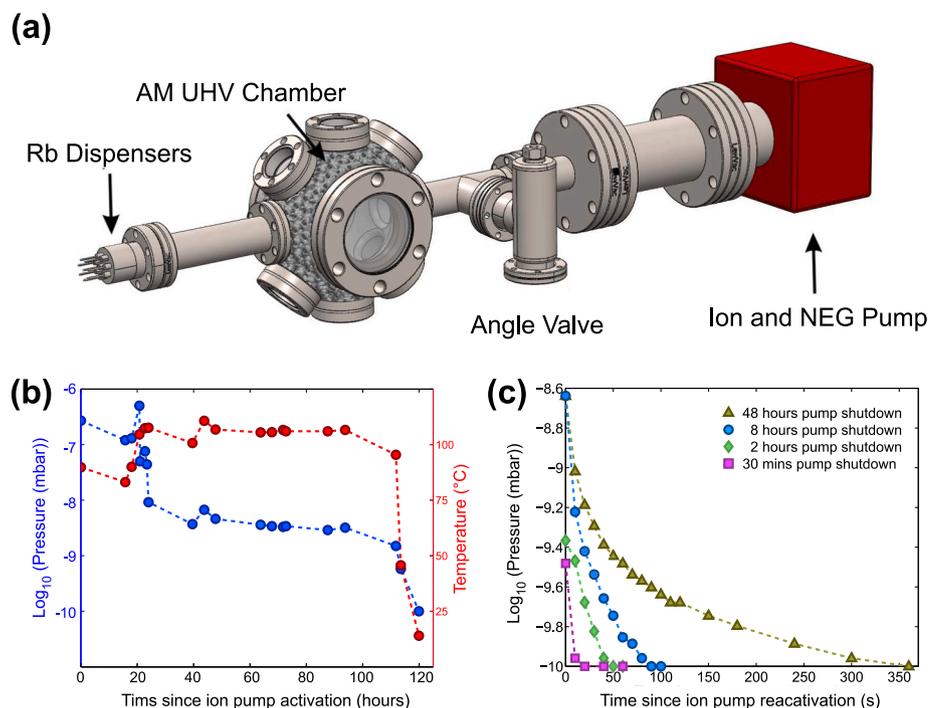
Fig. 5. UHV test setup and results (a) Schematic diagram illustrating the test setup of the vacuum system. For scale, the larger ports on the AM vacuum chamber are CF40 and the smaller CF16. (b) Pressure evolution (blue points) during bakeout (temperature represented by red points). (c) Recovery of vacuum after periods without active pumping. The pump contains a passive element (non-evaporable getters) and an active ion pump. The data shown are the pressures recorded following reactivation of the ion pump after a long period of only passive pumping. Note that the lower limit on the pressure that can be read is 10^{-10} mbar, and under-range readings are displayed as 10^{-10} mbar in both (b) and (c). Errors are $\pm 1.5\,°C$ in temperature and $\pm 10\%$ in pressure, the size of the markers exceeds the size of the error bars.

3. Results

A total of four chambers were produced via the methods described above, with visual inspection suggesting a similar build quality across all four. To test the performance resulting from the design and the surface characteristics, one finished chamber was assembled into a vacuum system using off-the-shelf stainless-steel viewports and tubes, mounted using standard CF flanges, as shown schematically in Fig. 5(a). Bake-out of the system was carried out for a period of 120 h, during which the temperature did not exceed 120°C. Once baked, the assembly was pumped using a combined ion / non-evaporable getter (NEG) pump (NEXTorr D100 − 5, SAES Getters) and was found to achieve a pressure in the UHV range. The ion pump current reading indicates a pressure $< 1 \times 10^{-10}$ mbar, the lower limit of what can be read using our device and close to the generally accepted reliability limit of ion-pump current measurements [43].

To place an upper limit on the total outgassing rate of the AM material we compare the achieved pressure to the pumping rate of the system. The pumping speed of the NEXTorr D100 − 5 is dependent upon the exact particle species being pumped; we consider the 40 l/s pumping speed applicable to nitrogen, as this is not only a common and plausible background gas constituent but also provides a mid-range pumping speed estimate likely to be broadly representative of the average properties of a multi-component residual gas. Based on this, and on the 11283 mm^2 nominal internal surface area of the AM vacuum chamber, we can place an upper limit on the outgassing rate of the AM vacuum chamber's internal surface of 3.6×10^{-13} mbar l/(s mm^2). While slightly above values typically measured for baked stainless steel, which are on the order of 5×10^{-14} mbar l/(s mm^2) [44], it is important to stress that this is only an upper limit on the material's outgassing rate. We have assumed that all of the gas pumped from the system originates from the AM material; this not only means that we determine the total gas load produced by the material, including micro-leaks and virtual leaks resulting from material porosity, but also that we underestimate the vacuum performance of the material by attributing to it all of the gas entering the system, when in fact contributions from the standard vacuum components connected to the AM chamber are likely to be substantial.

For a portable system, particularly relevant to quantum sensing applications, operation without external power supplies is highly desirable – therefore, the effect of turning off the ion pump for up to 48 h was tested. During this time span the chamber was pumped only via the passive NEG elements of the NEXTorr D100 − 5. When the ion pump was reactivated, the initial pressure was measured and its decay back to the under-range reading following ion pump activation was recorded.

The results of these tests are shown in Fig. 5(c). These tests demonstrate that the chamber can maintain pressures in the 10^{-10} mbar range for over two hours without active pumping and that even after 48 h, the pressure remains in the 10^{-9} mbar range. After the switch-on of the pump the chamber returns to below 10^{-10} mbar in less than 6 min. The background pressure achieved was more than sufficient to permit the capture of a cloud of cold Rb atoms in a magneto-optical trap. Fig. 1(b) shows a fluorescence image of the trapped atomic cloud, which contains up to 2×10^8 rubidium atoms. Loading times vary between < 1 s and ∼ 10 s, depending on the amount of Rb vapour dispensed into the chamber; this provides independent confirmation that the pressure is no higher than ∼ 5×10^{-9} mbar [45]. These values are typical of the performance of MOTs in conventional vacuum chambers and suggest the suitability of AM UHV equipment for use in portable quantum technologies.

Since the acquisition of these initial results a second of the four chambers has been assembled into a vacuum system and also achieves pressures in the UHV regime with comparable pumping speeds.

3.1. Technical details of assembly and bake-out

The chamber was cleaned before assembly — first with water and detergent, then with acetone and finally with isopropanol. Following this the chamber was attached to standard conflat vacuum components using standard silver-plated copper gaskets. The bolts used to close the joins and compress the gaskets secure directly into the machined bolt holes in the chamber itself. M6 bolts, tightened with a torque of 16 Nm, were used for the CF40 fittings and M4 bolts, tightened with a torque of 9 Nm, for the CF16. The assembled system was baked for 120 h at a maximum temperature of 120°C. During bake-out, a 300 l/s turbomolecular pump (Pfeiffer HiPace 300) was fitted via the angle valve shown

in Fig. 4(a).

4. Conclusions

In summary, we have demonstrated an additively manufactured vacuum chamber operating in the pressure range below 10^{-10} mbar and used it to trap a cold cloud of ^{85}Rb atoms. No degradation of the chamber's performance has been observed over several months of operation, and standard pumping methods appear able to sustain the stated pressure indefinitely. We described the design steps that lead to a significant reduction in weight while retaining stability and analyzed the surface structure and outgassing behaviour of the AM material. Introducing AM methods to UHV apparatus has enormous potential for reducing the size, weight and material consumption of existing systems and enabling new portable systems with increased functionality.

Promising areas for future investigation include the use of advanced lattice structures to increase passive cooling rates or enable external cooling, reduce eddy current generation in response to changes in magnetic field and damp or isolate mechanical vibrations. Another line of investigation is the use of AM to produce high surface area elements to enhance the efficiency of passive pumping devices such as Ti sublimation pumps. It may also be of interest to study the mechanism by which Mg enrichment of the surface layer occurs. If this is related to melt-pool dynamics [46] then the process will likely be common to many AM alloys, and could have broader implications for refinement of LPBF methodology. Finally, research into achieving comparable vacuum compatibility via alternative AM methodologies besides LPBF [34] may help to further broaden the options available for AM of UHV systems.

Declaration of Competing Interest

The authors have complied with Elsevier's ethical requirements. The presented work has not been published previously and is not under consideration for publication elsewhere. Also, its publication is approved by all authors and if accepted, it will not be published elsewhere in the same form, in any language, without the written consent of the Publisher. The authors do not have any conflicts of interest to declare.

Data Availability

All data necessary to support the conclusions are given in the article. All data collected as part of the research can be obtained from the authors upon reasonable request.

Appendix: mechanical testing

The durability of the knife-edges machined in the AlSi10Mg LPBF material was tested for repeated opening-closure cycles of a test flange. The performance of the seal was assessed using a leak detector (Pfeiffer Vacuum ASM 340). During all performed tests (up to 10 cycles) no measurable degradation of the seal was detected and the suitability of the selected post-processing heat treatment was thus confirmed. The performance of the threads machined into the blind holes was tested against the recommended bolt torque (9.5 Nm for M4, 16.3 Nm for M6 from Kurt J. Lesker) using standard stainless steel bolts within a similarly threaded test piece with M4 and M6 threaded holes. A torque wrench was used to apply the recommended bolt torque. No failure or noticeable degradation of the threads was observed.

Appendix A. Supporting information

Supplementary data associated with this article can be found in the online version at doi:10.1016/j.addma.2021.101898.

References

[1] P. Knight, et al., The Quantum Age: Technological Opportunities. Blackett Review, Government of Science, UK, 2016.

[2] K. Bongs, et al., The UK National Quantum Technologies Hub in sensors and metrology (Keynote Paper), Proc. SPIE 9900 (2016).

[3] S. Battersby, Core concept: quantum sensors probe uncharted territories, from earth's crust to the human brain, PNAS 116 (2019) 16663–16665.

[4] J. Kitching, S. Knappe, E. Donley, Atomic sensors - a review, IEEE Sens. J. 11 (2011) 1749–1758.

[5] I. Gibson, D. Rosen, B. Stucker, Additive Manufacturing for Technologies, Springer-Verlag, New York, 2015.

[6] D. Becker, et al., Space-borne Bose-Einstein condensation for precision interferometry, Nature 562 (2018) 391–395.

[7] S. Dimopoulos, et al., Gravitational wave detection with atom interferometry, Phys. Lett. B 678 (2009) 37–40.

[8] O. Carraz, et al., A spaceborne gravity gradiometer concept based on cold atom interferometers for measuring earthas gravity field, Microgravity Sci. Technol. 26 (2014) 139–145.

[9] L. Liu, et al., In-orbit operation of an atomic clock based on laser-cooled 87Rb atoms, Nat. Comm. 9 (2018), 2760.

[10] J.H. Martin, et al., 3D printing of high-strength aluminium alloys, Nature 549 (2018) 365–369.

[11] P. Barriobero-Vila, et al., Peritectic titanium alloys for 3D printing, Nat. Comm. 9 (2018), 3426.

[12] A.A. Martin, et al., Dynamics of pore formation during laser powder bed fusion additive manufacturing, Nat. Comm. 10 (2019), 1987.

[13] S.K. Everton, et al., Review of in-situ process monitoring and in-situ metrology for metal additive manufacturing, Mater. Des. 95 (2016) 431–445.

[14] E. Raab, et al., Trapping of neutral sodium atoms with radiation pressure, Phys. Rev. Lett. 59 (1987), 2631.

[15] S. Falke, et al., A strontium lattice clock with 3×10^{-17} inaccuracy and its frequency, N. J. Phys. 16 (2014), 073023.

[16] A.D. Ludlow, et al., Optical atomic clocks, Rev. Mod. Phys. 87 (2015) 637–701.

[17] F. Riehle, Optical clock networks, Nat. Photon. 11 (2017) 25–31.

[18] Y. Bidel, et al., Absolute marine gravimetry with matter-wave interferometry, Nat. Comm. 9 (2018), 627.

[19] W. Bin, et al., The investigation of a microgal-level cold atom gravimeter for field applications, Metrologia 51 (2014), 452.

[20] V. Menoret, et al., Gravity measurements below 10–9 g with a transportable absolute quantum gravimeter, Sci. Rep. 8 (2018), 12300.

[21] J.M. McGuirk, et al., Sensitive absolute-gravity gradiometry using atom interferometry, Phys. Rev. A 65 (2002), 033608.

[22] N. Behbood, et al., Real-time vector field tracking with a cold-atom magnetometer, Appl. Phys. Lett. 102 (2013), 173504.

[23] R. Saint, et al., 3D-printed components for quantum devices, Sci. Rep. 8 (2018), 8368.

[24] J. Vovrosh, et al., Additive manufacturing of magnetic shielding and ultra-high vacuum flange for cold atom sensors, Sci. Rep. 8 (2018), 2023.

[25] S. Jenzer, et al., Study of the suitability of 3D printing for ultra-high vacuum applications, Phys. Conf. Ser. 874 (2017), 012097.

[26] Z. Sun, G. Vladimirov, E. Nikolaev, L. Velasquez-Garcia, Exploration of metal 3-D printing technologies for the microfabrication of freeform, finely featured, mesoscaled structures, J. Micro Syst. 27 (2018) 1171–1185.

[27] C. Yang, L. Velasquez-Garcia, Low-cost, additively manufactured electron impact gas ionizer with carbon nanotube field emission cathode for compact mass spectrometry, J. Phys. D Appl. Phys. 52 (2018) 7.

[28] F. Motschmann, R. Gerard, F. Gilles, Purification of selective laser melting additive manufactured niobium for superconducting rf-applications transactions on applied superconductivity, IEEE Trans. Appl. Supercond. 29 (2019), 3500805.

[29] S. Jenzer, N. Delerue, Prospects of Additive Manufacturing for Accelerators.10th Int. Particle Accelerator Conf., 201910.18429/JACoW-IPAC2019-THPTS008.

[30] H.J. Metcalf, P. Van der Straten, Laser Cooling and Trapping, Springer-Verlag,, New York, 1999.

[31] I. Maskery, et al., Effective design and simulation of surface-based lattice structures featuring volume fraction and cell type grading, Mater. Des. 155 (2018) 220–232.

[32] D. Li, W. Liao, N. Dai, Y.M. Xie, Comparison of Mechanical Properties and Energy Absorption of Sheet-Based and Strut-Based Gyroid Cellular Structures with Graded Densities, Materials 12 (2019) 2183.

[33] B. Chen, et al., Strength and strain hardening of a selective laser melted AlSi10Mg alloy, Scr. Mater. 141 (2017) 45–49.

[34] S. Mirzababaei, S. Pasebani, A review on binder jet additive manufacturing of 316L stainless steel, J. Manuf. Mater. Process. 3 (2019) 82.

[35] L. Thijs, et al., Fine-structured aluminium products with controllable texture by selective laser melting of pre-alloyed AlSi10Mg powder, Acta Mater. 61 (2013) 1809–1819.

[36] N.T. Aboulkhair, et al., On the precipitation hardening of selective laser melted AlSi10Mg, Met. Mater. Trans. A 46 (2015) 3337–3341.

[37] N.T. Aboulkhair, et al., The microstructure and mechanical properties of selectively laser melted AlSi10Mg: the effect of a conventional T6-like heat treatment, Mat. Sci. Eng. A 667 (2016) 139–146.

[38] R.P. Campion, C.T. Foxon, R.C. Bresnahan, Modulated beam mass spectrometer studies of a Mark V Veeco cracker, J. Vac. Sci. Technol. B 28 (3) (2010).

[39] M. Tang, P.C. Pistorious, Oxides, porosity and fatigue performance of AlSi10Mg parts produced by selective laser melting, Int. J. Fatigue 94 (2017) 192–201.

[40] M. Simonelli, et al., A study on the laser spatter and the oxidation reactions during selective laser melting of 316L stainless steel, Al-Si10-Mg, and Ti-6Al-4V, Metall. Mater. Trans. A 46 (2015) 3842–3851.

[41] P. Sherwood, Introduction to studies of aluminium and its compounds by XPS, Surf. Sci. Spectra 5 (1) (1998).

[42] N. Haider, J. Alonso, W. Swartz, Valence and core electron spectra of Mg in MgO in evaporated thin films, Z. Naturforsch. A 30 (1975) 1485–1490.

[43] K. Welch, Capture pumping technology, Pergamon Press, 1991.

[44] C. Park, S. Kim, S. Ki, T. Ha, B. Cho, Measurement of outgassing rates of steels, J. Vis. Exp. 118 (2016), 55017.

[45] T. Arpornthip, C. Sackett, K. Hughes, Vacuum pressure measurements using a magneto-optical trap, Phys. Rev. A 85 (2012), 033420.

[46] S. Khairallah, A. Anderson, A. Rubenchik, W. King, Laser powder-bed fusion additive manufacturing: physics of complex melt flow and formation mechanisms of pores, spatter, and denudation zones, Acta Mater. 108 (2016) 36–45.